Inverse opal ceria–zirconia: architectural engineering for heterogeneous catalysis†

Grant A. Umeda,[a] William C. Chueh,[b] Liam Noailles,[a] Sossina M. Haile*[b] and Bruce S. Dunn[a]

Received 23rd June 2008, Accepted 22nd July 2008
First published as an Advance Article on the web 29th July 2008
DOI: 10.1039/b810641j

The application of inverse opal structured materials is extended to the ceria–zirconia ($Ce_{0.5}Zr_{0.5}O_2$) system and the significance of material architecture on heterogeneous catalysis, specifically, chemical oxidation, is examined.

Inverse opal structures have been explored and, in some instances, perfected as photonic crystals by the optoelectronics community.[1–4] Materials ranging from carbon to transition metal oxides have all been fabricated as macroporous structures with ordered pores.[5–7] In photonic applications, regular arrangement of the pore structure, with pore sizes generally in the visible wavelength range, is essential for achieving optical band gap characteristics. Inverse opals also display several characteristics that render them ideal for chemical and electrochemical catalysis including low tortuosity (particularly as compared to typical microporous materials[8] or to aerogels[9]), high porosity, and stability against high-temperature coarsening. Furthermore, the requirements for structural perfection are much less stringent than those of photonic applications, although a high degree of structural perfection ultimately lends itself to quantitative modeling of catalytic behavior to a degree not possible with conventional catalyst support structures. Despite these attributes, only a limited number of studies have been directed towards the development of inverse opals for catalysis,[10–12] and any influence of the material architecture has yet to be demonstrated.

Here, we report a robust method for preparing ceria–zirconia ($Ce_{0.5}Zr_{0.5}O_2$) inverse opals and provide preliminary catalytic results on the role of engineered macroscale porosity on catalytic activity. The synthesis of the end-member ceria as an inverse opal has been recently demonstrated,[13] however, the catalytic properties of that material were not examined. Ceria–zirconia, which combines the benefits of the catalytic activity[14] and oxygen storage capacity offered by ceria[15] and the structural stability offered by zirconia[16] was selected for this study because of its inherent importance in three-way catalysts for the destruction of toxic gases such as SO_x and NO_x,[17,18] as a support in ethanol reforming catalysts for hydrogen production,[19] and as an anode material in solid oxide fuel cells,[20] amongst many other applications. Furthermore, given the intermediate stoichiometry, the synthesis methodology lends itself to compositional tuning throughout the CeO_2–ZrO_2 system, as has already been demonstrated in the mesoporous analog.[8] We have utilized here a synthesis protocol (described in complete detail in the ESI†) by which a nanoparticulate sol is produced by reaction of zirconyl chloride and cerium ammonium nitrate.[21] Equal molar ratios are dissolved in deionized water and the products of the reaction are allowed to evaporate from the solution. The resulting precipitate, composed of 3–5 nm oxide particles, is resuspended in deionized water. The particles are then infiltrated into the interstices of a closed-packed array of 1.0 μm polystyrene (PS) beads prepared by sedimentation from an aqueous suspension. The beads are subsequently removed from the structure by thermal decomposition at 550 °C, a treatment which also induces the sintering of the nanoparticulate sol.

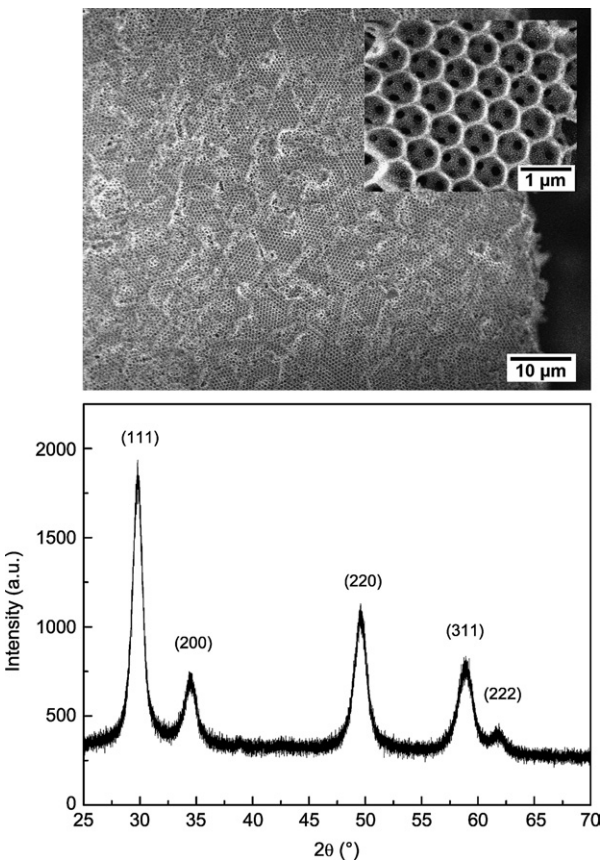

Fig. 1 (top) SEM image of the $Ce_{0.5}Zr_{0.5}O_2$ macroporous inverse opals showing the continuous oxide framework and pore network (inset), and (bottom) X-ray diffraction pattern, indexed, for simplicity, according to a cubic fluorite structure.

[a]*Department of Materials Science and Engineering, University of California, 405 Hilgard Ave, Los Angeles, CA 90095, USA*
[b]*Department of Materials Science, California Institute of Technology, 1200 E. California Blvd. M/C 309-81, Pasadena, CA 91125, USA. E-mail: smhaile@caltech.edu*

† Electronic supplementary information (ESI) available: Synthesis protocol: Materials, characterization and catalytic reactions. See DOI: 10.1039/b810641j

The resulting macroporous ceria–zirconia microstructure and corresponding diffraction pattern are shown in Fig. 1. The scanning electron microscopy (SEM) image shows a continuous oxide framework with an interconnected pore network that permeates throughout the structure. The pore interconnections (average diameter 160 nm) reflect the degree of contact between the polystyrene beads obtained during the formation of the opal structure. The X-ray diffraction pattern confirms that a fluorite phase is obtained, and the peak breadths indicate a crystallite size of $\sim$ 20 nm after the 500 °C heat treatment. As a result of the highly broadened peaks, structural refinement according to cubic and tetragonal fluorite structures yielded statistically equivalent fits, although a minor peak at $2\theta \sim 39°$ can only be accounted for by the tetragonal form. The refined tetragonal lattice constants, a = 3.6654(9) Å and c = 5.263(2) Å, are consistent with the nominal composition of $Ce_{0.5}Zr_{0.5}O_2$. Chemical analysis by energy dispersive X-ray analysis shows a residual Cl level that is below the quantification limit of the technique (<0.5 wt%). Nitrogen sorption measurements indicate the material has a moderate specific surface area, 13.6 $m^2\ g^{-1}$. In contrast, non-templated ceria–zirconia powder obtained from direct heat treatment of the precipitate resulting from the chemical synthesis displayed a specific surface area of 38.3 $m^2\ g^{-1}$.

In order to explore the role of material architecture on catalytic activity a propane oxidation experiment (for details see the ESI†) was performed. Measurements were carried out using a $C_3H_8 : O_2$ ratio of 1 : 2.25 ($P_{C_3H_8}$ = 0.009 atm, P_{O_2} = 0.021 atm, balance He, total flow rate = 130 sccm), which is slightly greater than that required for partial oxidation (to generate entirely CO and H_2) but substantially lower than that required for complete oxidation (to generate entirely CO_2 and H_2O). At the flow rates employed the reaction is gas-phase transport limited. The catalytic activity of the non-templated ceria–zirconia powder (50 mg) has a propane conversion curve comparable to the control (quartz sand only), Fig. 2, suggesting that it is relatively inactive towards the heterogeneous catalytic oxidation of propane. In both the control and non-templated powder cases, the conversion at 500 °C is only 2–3%, and at temperatures above 550 °C propane oxidation directly in the gas phase can no longer be neglected. The macroporous inverse opal catalyst, on the other hand, displayed a significantly higher catalytic activity and the conversion at 500 °C is nearly 23%. Given the essentially identical solution synthesis routes employed and higher specific surface area of the non-templated ceria–zirconia powder over the macroporous material, the behavior of the latter cannot be attributed to the presence of a particularly high concentration of catalytic sites or substantially differing impurity levels and must derive, in large part, from the macroporosity. To further examine the role of *ordered* macroporosity, the ceria–zirconia inverse opal was ground to partially disrupt the ordered structure while retaining most of its macroporosity. Considerably lower propane conversion (14% at 500 °C) than the undisturbed material can be attributed to increased tortuosity in the gas transport pathway. The results above clearly demonstrate the strong influence of material architecture on catalytic behavior.

For any high temperature process, and particularly where the component materials have high porosity and surface area, the question of long-term stability must be addressed. Here we see that under continuous operation at 550 °C ($P_{C_3H_8}$ = 0.028 atm, P_{O_2} = 0.062 atm, balance He, total flow rate = 195 sccm), Fig. 3, propane conversion drops slightly over the first 45 h from 35 to 26% then remains stable through the remainder of the 100 h experiment. The X-ray diffraction patterns between the pre-reaction and post-reaction materials showed no difference in the crystal structure or the crystallite size. SEM observations of the post-reaction sample also confirmed that the catalyst microstructure was essentially unchanged, although some small fraction of pores appeared to have collapsed. Overall, the minimal degradation rate beyond about 50 h demonstrates promising stability for catalytic applications.

Examination of the exhaust gas obtained from the macroporous ceria–zirconia revealed that, at temperatures below which gas-phase reactions occur, the main products were H_2O and CO_2 (and unreacted propane) with minimal amounts of H_2 and CO (see ESI†). Furthermore, there was no indication of carbon deposition. Such a result does not align with thermodynamic equilibrium, however, similar behavior has been documented recently for Pt catalyzed oxidation of propane under comparable experimental conditions.[22] Complete oxidation under fuel rich conditions has important implications for the destruction of volatile organic compounds and for catalytic heat sources.[23,24]

Beyond chemical catalysis, the macroporous structure prepared here displays several desirable characteristics for application in fuel cell electrodes, *i.e.* for electrocatalysis. In contrast to the random

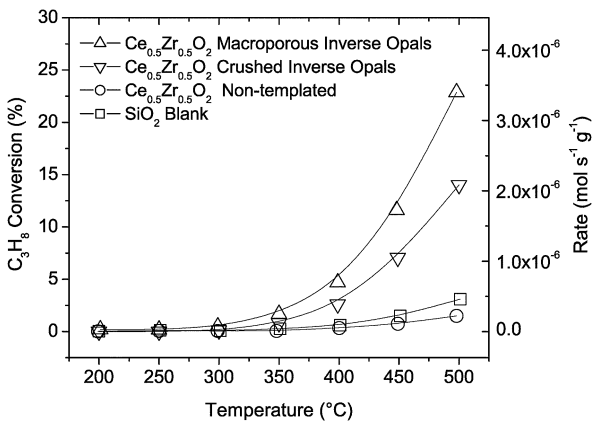

Fig. 2 Propane conversion for $Ce_{0.5}Zr_{0.5}O_2$ macroporous inverse opals, crushed inverse opals, non-templated powders, and SiO_2 blank. $P_{C_3H_8}$ = 0.009 atm, P_{O_2} = 0.021 atm, balance He, total flow rate = 130 sccm.

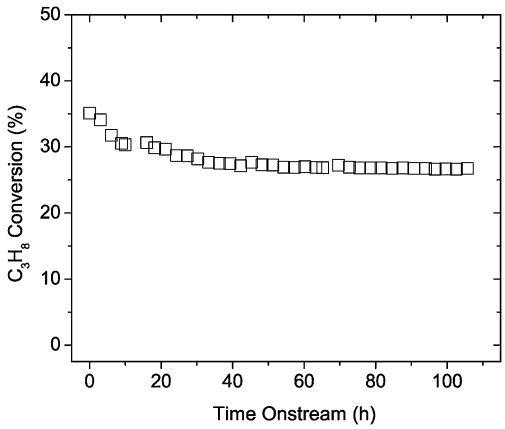

Fig. 3 Propane conversion degradation for $Ce_{0.5}Zr_{0.5}O_2$ macroporous inverse opals under continuous operation at 550 °C for 100 h. $P_{C_3H_8}$ = 0.028 atm, P_{O_2} = 0.062 atm, balance He, total flow rate = 195 sccm.

structure of typical composite electrodes,[25] not only does the ordered macroporosity facilitate mass transport as a consequence of the low tortuosity, but also the walls of the inverse opal provide a continuous pathway for oxygen ion transport. Hence, the entirety of the electrolyte material within the electrode is, in principle, electrochemically accessible. Implementation of CeO_2–ZrO_2 based inverse opals in functioning fuel cell anodes will ultimately require the incorporation of a second phase that is both electronically conducting and microstructurally continuous, but the success demonstrated here represents an essential first step towards engineered rather than random electrode architectures.

Regardless of the specific application, it is apparent that material architecture is an important but relatively unexplored parameter (in addition to overall composition and surface state) that one can tune in order to optimize catalytic conversions relevant to energy generation and emission control technologies. The inverse opal structure, because of the ease by which it can be fabricated and the ease with which its dimensional characteristics—pore size, interconnecting pore size, wall thickness, and constituent grain size—can be varied, is an ideal framework for pursuing such an optimization. The regularity of the structure further suggests that such optimization can proceed in parallel with computational simulations, which are typically better suited to well-defined than random structures.

Notes and references

1 B. T. Holland, C. F. Blanford and A. Stein, *Science*, 1998, **281**, 538–540.
2 O. D. Velev, T. A. Jede, R. F. Lobo and A. M. Lenhoff, *Nature*, 1997, **389**, 447–448.
3 J. E. G. J. Wijnhoven and W. L. Vos, *Science*, 1998, **281**, 802–804.
4 Y. N. Xia, B. Gates and Z. Y. Li, *Adv. Mater.*, 2001, **13**, 409–413.
5 B. T. Holland, C. F. Blanford, T. Do and A. Stein, *Chem. Mater.*, 1999, **11**, 795–805.
6 K. T. Lee, J. C. Lytle, N. S. Ergang, S. M. Oh and A. Stein, *Adv. Funct. Mater.*, 2005, **15**, 547–556.
7 J. S. Sakamoto and B. Dunn, *J. Mater. Chem.*, 2002, **12**, 2859–2861.
8 T. Brezesinski, M. Antonietti, M. Groenewolt, N. Pinna and B. Smarsly, *New J. Chem.*, 2005, **29**, 237–242.
9 M. A. Thundathil, W. Lai, L. Noailles, B. S. Dunn and S. M. Haile, *J. Am. Ceram. Soc.*, 2004, **87**, 1442–1445.
10 C. X. Fanlin Chen and Meilin Liu, *Chem. Lett.*, 2001, 1032–1033.
11 G. Q. Guan, R. Zapf, G. Kolb, Y. Men, V. Hessel, H. Loewe and J. H. Ye, *Chem. Commun.*, 2007, 260–262.
12 P. J. A. K. Michael Mitchell Christian, *Lab Chip*, 2006, **6**, 1328–1337.
13 T. W. Wang, O. Sel, I. Djerdj and B. Smarsly, *Colloid Polym. Sci.*, 2006, **285**, 1–9.
14 W. Lai and S. M. Haile, *J. Am. Ceram. Soc.*, 2005, **88**, 2979–2997.
15 A. Trovarelli, *Catal. Rev. Sci. Eng.*, 1996, **38**, 439–520.
16 M. Ozawa, *J. Alloys Compd.*, 2006, **408–412**, 1090–1095.
17 C. Hori, H. Permana, K. Ng, A. Brenner, K. More, K. Rahmoeller and D. Belton, *Appl. Catal., B*, 1998, **16**, 105–117.
18 J. Kaspar, P. Fornasiero and M. Graziani, *Catal. Today*, 1999, **50**, 285–298.
19 J. Breen, R. Burch and H. Coleman, *Catal. Rev. Sci. Eng.*, 2002, **39**, 65–74.
20 B. Steele, *Nature*, 1999, **400**, 619.
21 M. Hirano, T. Miwa and M. Inagaki, *J. Solid State Chem.*, 2001, **158**, 112–117.
22 W. C. Chueh, Z. Shao and S. M. Haile, *Top. Catal.*, 2007, **46**, 402–413.
23 J. Ahn, C. Eastwood, L. Sitzki and P. D. Ronney, *Proc. Combust. Inst.*, 2005, **30**, 2463–2372.
24 J. Vican, B. F. Gajdeczko, F. L. Dryer, D. L. Milius, I. A. Aksay and R. A. Yetter, *Proc. Combust. Inst.*, 2002, **29**, 909.
25 J. R. Wilson, W. Kobsiriphat, R. Mendoza, H. Y. Chen, J. M. Hiller, D. J. Miller, K. Thornton, P. W. Voorhees, S. B. Adler and S. A. Barnett, *Nat. Mater.*, 2006, **5**, 541–544.